Journal of Sound and Vibration 373 (2016) 205–222

Contents lists available at ScienceDirect

Journal of Sound and Vibration

journal homepage: www.elsevier.com/locate/jsvi

An analytical approach for predicting the energy capture and conversion by impulsively-excited bistable vibration energy harvesters

R.L. Harne [a,*,1], Chunlin Zhang [b,c,1], Bing Li [b], K.W. Wang [c]

[a] Department of Mechanical and Aerospace Engineering, The Ohio State University, Columbus, OH 43210, USA
[b] State Key Laboratory for Manufacturing and Systems Engineering, Xi'an Jiaotong University, Xi'an, Shaanxi 710049, PR China
[c] Department of Mechanical Engineering, University of Michigan, Ann Arbor, MI 48109, USA

ARTICLE INFO

Article history:
Received 1 July 2015
Received in revised form
24 January 2016
Accepted 9 March 2016
Handling Editor: W. Lacarbonara
Available online 29 March 2016

Keywords:
impulse excitation
impulsive vibrations
vibration energy harvesting
bistable oscillator
structural dynamics

ABSTRACT

Impulsive energies are abundant throughout the natural and built environments, for instance as stimulated by wind gusts, foot-steps, or vehicle–road interactions. In the interest of maximizing the sustainability of society's technological developments, one idea is to capture these high-amplitude and abrupt energies and convert them into usable electrical power such as for sensors which otherwise rely on less sustainable power supplies. In this spirit, the considerable sensitivity to impulse-type events previously uncovered for bistable oscillators has motivated recent experimental and numerical studies on the power generation performance of bistable vibration energy harvesters. To lead to an effective and efficient predictive tool and design guide, this research develops a new analytical approach to estimate the electroelastic response and power generation of a bistable energy harvester when excited by an impulse. Comparison with values determined by direct simulation of the governing equations shows that the analytically predicted net converted energies are very accurate for a wide range of impulse strengths. Extensive experimental investigations are undertaken to validate the analytical approach and it is seen that the predicted estimates of the impulsive energy conversion are in excellent agreement with the measurements, and the detailed structural dynamics are correctly reproduced. As a result, the analytical approach represents a significant leap forward in the understanding of how to effectively leverage bistable structures as energy harvesting devices and introduces new means to elucidate the transient and far-from-equilibrium dynamics of nonlinear systems more generally.

1. Introduction

The conversion of ambient vibrations into a usable electric power resource has motivated a broad range of interests [1,2], where one common goal is to leverage the converted energies to realize self-powered electronics that otherwise rely on less sustainable powering methods. The characteristics of the vibration resources vary considerably, from strongly harmonic motions like those induced by rotating machinery [3], to purely stochastic oscillations [4–7] like the heaving of ocean waves

* Corresponding author.
E-mail address: harne.3@osu.edu (R.L. Harne).
[1] These authors contributed equally to this work.

http://dx.doi.org/10.1016/j.jsv.2016.03.012
0022-460X/

[8,9], and transient vibrations like those resulting from moving vehicles on roadways [10,11]. Impulsive motions form an important subset of the ambient, transient vibration resources: they are high-amplitude energies suddenly transmitted in brief durations of time. Oscillations induced due to human activities are oftentimes impulsive: walking or running individuals cause shocks to their portable electronic devices [12,13], automobiles driven over traffic counters or speed bumps induce local impulsive forces on the counters or road surface [14], and extensive research illustrates the impulsive nature of forces exerted upon stairs due to human walking [15]. For the beneficial applications of energy harvesters in impulsive excitation environments (e.g., charging electronics borne and jolted by jogging individuals, self-powered traffic monitoring systems, to name a few), the deployment of a suitable vibration energy harvester is critical to maximize device sensitivity to the impulsive excitations.

Recent research has shown that *bistable* energy harvesters are particularly sensitive to impulsive inputs [14,16–19]. Fig. 1 (a) and (b), respectively, show a prototypical bistable, piezoelectric energy harvester and its schematic model for oscillations that strictly exhibit fundamental mode behaviors. In agreement with our experimental system described in Section 5, the inducement of bistability illustrated in Fig. 1(a) is by mutual attractions between the ferromagnetic cantilever substrate and a base-mounted magnet pair. Fig. 1(c) provides an exemplary representation of the vibrations of the bistable harvester when excited by an impulse of initial relative velocity between the tip mass and the base. These numerically simulated results illustrate that the transient oscillations of the bistable harvester are characterized by two distinct regimes: an initial phase of *snap-through* oscillation where the inertial mass vibrates between the two stable equilibria, followed by a period of ring-down-type *intrawell* vibrations at the end of which the bistable device returns to a resting position. The lower inset of Fig. 1 shows that the net converted energy (the integration of instantaneous electrical power in time) is more than an order of magnitude greater for the few cycles of snap-through oscillation than that generated by the long-time intrawell dynamics.

This finding motivates the development of an accurate and efficient predictive tool to determine the power generation performance resulting from the favorable snap-through oscillations induced due to impulsive excitations. Such a tool might then inform and guide design and implementation of bistable vibration energy harvesters excited in impulsive motion environments, so as to enhance device sensitivity to the properties of the anticipated impulsive vibration resource. The aim of this research is to develop such a predictive strategy and thus design tool.

Numerical simulations, for example the Runge–Kutta algorithm-based approach used to generate the representative results in Fig. 1, are one means to estimate the power generation of a bistable energy harvester excited by impulses. However, these strategies are computationally-expensive. In other words, each simulation is an indicator of performance for only one set of design parameters and one prescribed impulsive event. A predictive approach based upon an analytical formulation of the impulsively-excited dynamics of a bistable energy harvester is preferred for the more generalized character of the results and the ease in carrying out the computations of detailed and insightful parametric studies.

In fact, many researchers have devised analytical strategies to predict the transient dynamics of bistable oscillators in the absence of electromechanical coupling. Lakrad and Belhaq [20] developed an approach to approximate the *free, undamped* oscillations of bistable structures, and Yuste and Bejarano [21], Yuste [22], Cveticanin [23], and Al-Shudeifat [24] devised different means to predict the *transient, dissipative* dynamics of bistable oscillators. Although lacking the inclusion of electromechanical influences, these latter approaches are of importance to the current investigation in the broader dynamical sense. On the other hand, these advancements have limitations since the predictions may be accurate for only a few cycles of oscillation and may exhibit severe parameter sensitivity in the fidelity of the estimates.

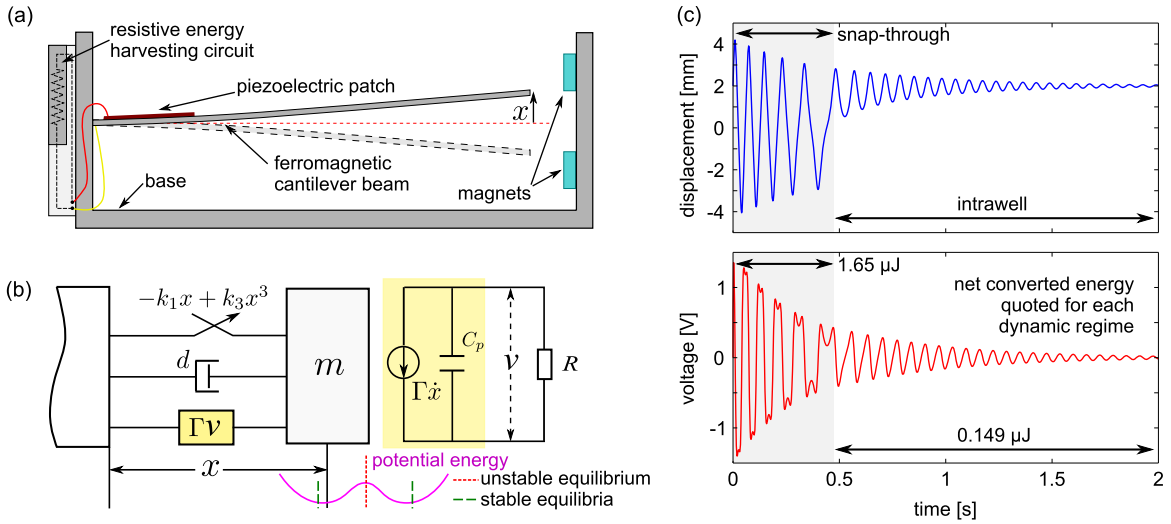

Fig. 1. (a) A prototypical bistable, piezoelectric energy harvesters under impulsive excitation upon the relative motion between beam tip and base; (b) schematic model of the bistable harvester in (a); and (c) an exemplary simulation of the bistable vibration energy harvester beam tip displacement and transduced voltage induced by an impulsive input of relative velocity between the base and harvester beam tip.

To surmount such challenges for the high-fidelity prediction of electromechanical dynamics exhibited by impulsively-excited bistable energy harvesters, a promising idea is to harness a framework composed from the averaging method and Jacobian elliptic functions [25]. Coppola and Rand [26,27] approximated the transient dynamics of *monostable*, nonlinear oscillators using such tools, which was the tactic likewise employed by Belhaq and Lakrad [28]. Yet, for *bistable* oscillators, the near-identity transformation underlying the classical averaging method [29] favors accurate predictions only in the event that the bistable structure oscillates with small displacements near one of the two stable equilibria. In the current interest of effective bistable energy harvester development for impulsive excitation environments, the prediction of the large-amplitude, power-generating snap-through vibrations necessitates a new approach not inhibited by such restrictions.

The research presented in this paper tackles the aforementioned challenges by developing a new analytical approach for predicting the transient dynamics of bistable vibration energy harvesters, both near- and far-from-equilibrium. To this end, the Jacobian elliptic functions are employed in the averaging method that is enhanced by relaxing assumptions regarding the degree of time-varying dynamic amplitudes. The following sections review the mathematical formulation of the bistable harvester and the procedures undertaken to analytically predict the transient electromechanical dynamics as well as to compute the average power generation achieved for a prescribed excitation impulse. The accuracy of the approach is assessed, in a strict sense, by comparison with numerically simulated results which are considered to be the exact dynamics. The analytical predictions are also validated through comparison with an extensive set of experimental findings. Finally, the advancements of this research are summarized and future directions are highlighted.

2. Governing equations for the bistable vibration energy harvester

Similar to the cantilevered, piezoelectric energy harvesting beam illustrated in Fig. 1, the bistability of the cantilever is assumed to be induced by applied axial compressive force mechanisms, such as geometric constraints or by repulsive or attractive magnet pairs. In such events, it is well-established that the governing equations of motion are formulated according to the primary generalized displacement and the voltage across an attached external (resistive) load. By such a model formulation regarding the combined elastic and applied restoring force effects, the net restoring force approximation for the structural dynamics includes negative linear and positive cubic stiffnesses [30–33]. The convention of considering the external circuit as a purely resistive load follows the knowledge that the influence of more intricate power conditioning stages may be sufficiently captured using the lumped resistance model [34]. Also, the absence of coupling to underlying, exciting structural dynamics (such as a base structure to which the harvester is attached) is consistent with the assumptions that the underlying structure is sufficiently massive with respect to the inertia of the harvester [1]. These equations of motion are expressed using

$$\begin{cases} m\ddot{x}+\mathrm{d}\dot{x}-k_1x+k_3x^3+\Gamma v=0 \\ C_p\dot{v}+v/R=\Gamma\dot{x} \\ x|_{t=0}=x_0,\ \ \dot{x}|_{t=0}=\dot{x}_0,\ \ v|_{t=0}=0 \end{cases} \tag{1}$$

where x is the generalized displacement of the piezoelectric cantilever (here, indicating the relative motion between the beam tip and the base to which it is clamped); v is the voltage across a load resistance R; m is the inertial mass; d is a damping constant; k_i $(i=1,\ 3)$ are stiffness constants; C_p is the capacitance of the piezoelectric layers; and Γ is the electromechanical coupling constant. The structure exhibits one of two stable equilibria displacements $x^*=\pm\sqrt{k_1/k_3}$ m, which are here assumed to be symmetric about an unstable equilibrium $x^*=0$ m. Assuming the piezoelectric cantilever is initially at rest with configuration $x^*=\sqrt{k_1/k_3}$ m, the initial velocity $\dot{x}|_{t=0}=\dot{x}_0$ m.s^{-1} is chosen to reflect an impulsive excitation according to the impulse-momentum theorem. After introduction of the following parameters

$$\gamma=d/m;\quad \alpha=k_1/m;\quad \beta=k_3/m;\ \rho=\ 1/RC_p;\ \theta=\ \Gamma/C_p;\ \varepsilon=\ C_p/m \tag{2}$$

the governing equations are cast into a more general form [35]:

$$\begin{cases} \ddot{x}+\gamma\dot{x}-\alpha x+\beta x^3+\varepsilon\theta v=0 \\ \dot{v}+\rho v=\theta\dot{x} \\ x|_{t=0}=x^*,\ \ \dot{x}|_{t=0}=\dot{x}_0,\ \ v|_{t=0}=0 \end{cases} \tag{3}$$

Of note, ρ is the electromechanical time constant while θ may be described as a transduction or electromechanical coupling constant. Finally, the linear natural frequency is calculated with respect to the linear oscillations around one of the stable equilibria: $\sqrt{2k_1/m}$ [29].

3. Analytical prediction of the conservative vibrations of a bistable oscillator

To analytically estimate the transient dynamics of bistable harvesters using Jacobian elliptic functions, it is essential to determine the time-varying argument and modulus of the elliptic functions, which directly influence the time-varying displacement and voltage amplitudes. In this section, the argument and modulus of the elliptic function are derived to be

functions of the displacement amplitude in the conservative case. These relations become foundational in the predictions of transient, electromechanical dynamics of bistable energy harvesters as developed in Section 4.

The Jacobian elliptic functions are known to exactly describe the snap-through and intrawell vibration responses of unforced and undamped bistable oscillators [29,36], meaning that $\gamma=\theta=0$. The generalized displacement is expressed using

$$x_i=\zeta_i M_{i0}ep(\omega_i t+\varphi_{i0},k_i)=\zeta_i M_{i0}ep(u_i,k_i)\equiv\zeta_i M_{i0}ep_i,\quad i=c,d \tag{4}$$

where subscript $i=c,d$ represents the dynamic regime such that c denotes snap-through and d indicates intrawell behaviors. ζ_i are functions described below. M_{i0} are amplitudes of the generalized displacement. The functions ep_i are Jacobian elliptic functions given by $ep_c=cn(u_c,k_c)\equiv cn_c$ for snap-through and $ep_d=\mathrm{d}n(u_d,k_d)\equiv \mathrm{d}n_d$ for intrawell oscillation. The argument is $u_i=\omega_i t+\varphi_{i0}$ where ω_i is the frequency, while the modulus is k_i. In what follows, the argument and modulus of the elliptic functions are distinct whether considering the snap-through or intrawell dynamic regimes. As such, the subscript c indicates that the argument u_c and modulus k_c are taken in the evaluations of sn_c, cn_c, $\mathrm{d}n_c$, and Z_c. Likewise, subscript d denotes that the argument u_d and modulus k_d are employed to evaluate sn_d, cn_d, $\mathrm{d}n_d$, and Z_d in the intrawell regime. The elliptic functions ep_i have period T_i given by $T_c=4K(k_c)$ and $T_d=2K(k_d)$, where $K(k_i)$ is the complete elliptic integral of the first kind [37]. These functions reduce to $ep_c=cn(u_c,0)=\cos(u_c)$ and $ep_d=\mathrm{d}n(u_d,0)=1$ for the special case of a null modulus. The first and second order derivatives of x_i are, respectively,

$$\dot{x}_i=\frac{\mathrm{d}x_i}{\mathrm{d}(ep_i)}\cdot\frac{\mathrm{d}(ep_i)}{\mathrm{d}u_i}\cdot\frac{\mathrm{d}u_i}{\mathrm{d}t}=\zeta_i M_{i0}\omega_i ep_i' \tag{5a}$$

$$\ddot{x}_i=\zeta_i M_{i0}\omega_i\cdot\frac{\mathrm{d}(ep_i')}{\mathrm{d}u_i}\cdot\frac{\mathrm{d}u_i}{\mathrm{d}t}=\zeta_i M_{i0}\omega_i^2\left[\rho_{i1}ep_i+\rho_{i3}ep_i^3\right] \tag{5b}$$

where $\rho_{c1}=2k_c^2-1$; $\rho_{c3}=-2k_c^2$; $\rho_{d1}=2-k_d^2$; $\rho_{d3}=-2$. Substituting Eq. (5) into (3) with $\gamma=\theta=0$ leads to the relations between the instantaneous displacement amplitude M_{i0} and ω_i^2 or k_i. Note that for the conservative system lacking electromechanical coupling, the values of ω_i^2 and $k_i$are constants. For intrawell vibration

$$\omega_d^2=\beta M_{d0}^2/2;\ k_d^2=2-2\alpha/\left(\beta M_{d0}^2\right) \tag{6}$$

while for snap-through vibration

$$\omega_c^2=\beta M_{c0}^2-\alpha;\ k_c^2=\beta M_{c0}^2/\left[2\left(\beta M_{c0}^2-\alpha\right)\right] \tag{7}$$

Thus, for the undamped and uncoupled system, the intrawell and snap-through oscillations are given by, respectively,

$$x_d=\zeta_d M_{d0}\cdot dn\left(\sqrt{\beta M_{d0}^2/2}\cdot t+\varphi_{d0},\left[2-2\alpha/\left(\beta M_{d0}^2\right)\right]^{1/2}\right) \tag{8a}$$

$$x_c=\zeta_c M_{c0}\cdot cn\left(\sqrt{\beta M_{c0}^2-\alpha}\cdot t+\varphi_{c0},\left[\beta M_{c0}^2/\left(2\left(\beta M_{c0}^2-\alpha\right)\right)\right]^{1/2}\right) \tag{8b}$$

The term ζ_c is always equal to unity. In contrast, ζ_d relates to the stable equilibrium around which the intrawell oscillations occur:

$$\zeta_d=\begin{cases}sgn[x_0], & if\ \ x_0\neq 0\\ sgn[\dot{x}_0], & if\ \ x_0=0\end{cases} \tag{9}$$

The initial displacement and velocity at the time $t=0$ satisfy $x_0=\zeta_i M_{i0}ep_i$and $\dot{x}_0=\zeta_i M_{i0}\omega_i ep_i'$, respectively. Consequently, the initial amplitude and phase are determined from

$$M_{i0}=\beta^{-1/2}\cdot\left(\alpha+\sqrt{\left(\alpha-\beta x_0^2\right)^2+2\beta\dot{x}_0^2}\right)^{1/2} \tag{10a}$$

$$ep_i'(\varphi_{i0},k_i)/ep_i(\varphi_{i0},k_i)=\dot{x}_0/(\omega_i x_0) \tag{10b}$$

For the Jacobian elliptic function $ep_i(u,k)$, the modulus is constrained to $0\le k^2\le 1$. By Eq. (8), for intrawell oscillations this constraint leads to $1/2\le\ \alpha/\left(\beta M_{d0}^2\right)\le 1$ while $0\le\alpha/\left(\beta M_{c0}^2\right)\le 1/2$ results from application of the constraint in the context of snap-through vibration. Using the developments above, the system Hamiltonian is expressed to determine the instantaneous energy

$$E_i=\dot{x}_i^2/2-\alpha x_i^2/2+\beta x_i^4/4=M_{i0}^2\left(\beta M_{i0}^2-2\alpha\right)/4 \tag{11}$$

According to the above constraints on $\alpha/\beta M_{i0}^2$, when the instantaneous system energy is negative, the bistable oscillator (recalling that it is neither electromechanically coupled $\theta=0$ nor damped $\gamma=0$) undergoes intrawell oscillations. For positive instantaneous system energy, snap-through vibrations occur. Therefore, once dissipative and electromechanically

coupled dynamics are accounted for in the new analytical formulation derived below for the bistable energy harvester, the critical condition $\beta M_i^2 = 2\alpha$ denotes the boundary between the transient, decaying snap-through vibrations from the intrawell oscillations which occur later in time, such as that transition shown in Fig. 1. Yet to predict such behaviors, a more capable analytical framework is required than the developments [29,36] reviewed above.

4. Analytical formulation for the transient, damped dynamics and converted energy

Following the expressions established in Section 3, this section builds the analytical tools required to estimate the transient dynamics and harvested power of impulsive-excited and damped bistable energy harvester. For the dissipative system expressed using Eq. (3), the transient oscillations may exhibit periods of snap-through motions followed by intrawell behaviors such as that illustrated from the numerical example of Fig. 1(c). This apparently implies that the dynamical features of the system are transient in nature. To meet this obvious requirement, the amplitude $M_i = M_i(t)$ and argument $u_i = T_i\psi_i(t)$ are assumed to be slowly varying in time (where $T_i\psi_i$ is conceived to be a phase), while constraints on the modulus as derived in Section 3 must still be met. Therefore, the transient vibrations satisfying Eq. (3) are expressed using

$$x_i = \zeta_i M_i(t) ep_i(u_i, k_i) = \zeta_i M_i(t) ep_i\left(T_i\psi_i, k_i\right) = \zeta_i M_i(t) ep_i\left(\sigma_i K_i\psi_i, k_i\right) \equiv \zeta_i M_i(t) ep_i, \quad i = c, d \tag{12a}$$

$$\dot{x}_i = \zeta_i M_i \omega_i ep_i' \tag{12b}$$

$$\omega_c^2 = \beta M_c^2 - \alpha;\ \omega_d^2 = \beta M_d^2/2;\ k_c^2 = \beta M_c^2/\left[2\left(\beta M_c^2 - \alpha\right)\right];\ k_d^2 = 2 - 2\alpha/\left(\beta M_d^2\right) \tag{12c}$$

Here, $u_i = T_i\psi_i$ is used as the argument; T_i is the period of the Jacobian elliptic function ep_i and thus $\sigma_c = 4$ and $\sigma_d = 2$; $\zeta_c \equiv 1$ and $\zeta_d = \pm 1$ as defined in Section 3. Unlike the conservative and uncoupled system detailed in Section 3, in the case of the damped and coupled platform, the values of ω_i^2 and k_i^2 vary in time according to their dependence upon M_i^2.

The rest of this section is structured as follows. In Section 4.1, the relation between the transduced voltage and the structural dynamic response is established, which simplifies the governing equation formulation to facilitate the continuing derivation. Through the connections found in Eq. (12c) between the elliptic function variables and the displacement amplitude M_i, Section 4.2 derives an implicit expression of the vibration amplitude using the averaging method. The exact expression of the amplitudes M_i are satisfactorily simplified in Section 4.3 to enable an integration of the equation that yields a closed form expression. In Section 4.4, the instantaneous vibration frequency components are subsequently determined from the time-varying displacement amplitudes. This information thereafter enables one to find the instantaneous trajectories of the harvester displacement, velocity, and voltage, according to the derivation and results given in Section 4.5. The final step is given in Section 4.6 where the instantaneous electric power and net converted energy are expressed according to the time-varying amplitudes M_i.

4.1. Transduced voltage coupling relation to the structural dynamic response

Apart from strongly coupled piezoelectric systems or those operating at frequencies close to the time constant of the piezoelectric capacitance and attached electrical load [38,39], the primary influence of the piezoelectric and electrical coupling upon the structural dynamics is a dissipative effect. Such a reduction of role is particularly relevant in the context of utilizing structures which employ nonlinearities that reduce the net linear stiffnesses to small values [40], such as weak bistability properties which are prime to be leveraged for energy harvesting from ambient impulses. Taking such factors into account, the induced voltage is assumed to be proportional to the velocity $v_i = A_i\dot{x}_i, \quad i = c, d$. Here, A_i is a coefficient determined as follows. The first order derivative of v_i is

$$\dot{v}_i = \dot{A}_i\dot{x}_i - A_i\left(\gamma\dot{x}_i - \alpha x_i + \beta x_i^3 + \varepsilon\theta v_i\right) \tag{13}$$

Using these relations in the third equation of Eq. (3), one obtains

$$\dot{A}_i\dot{x}_i = \left[\varepsilon\theta A_i^2 - (\rho - \gamma)A_i + \theta\right]\dot{x}_i - \alpha A_i x_i + \beta A_i x_i^3 \tag{14}$$

The method of averaging is then employed over one period of transient oscillation (i.e., a period of T_i with respect to argument u_i). In this way, the averaged variable is the smooth, local mean of the variable; hereafter this and related averaged variables are referred to as "averaged instantaneous" variables. First, ep_i' is multiplied to both sides of Eq. (14) and the equation is averaged to yield

$$\frac{1}{T_i}\int_0^{T_i} \dot{A}_i\dot{x}_i ep_i' \mathrm{d}u_i = \frac{1}{T_i}\int_0^{T_i} \left(\left[\varepsilon\theta A_i^2 - (\rho - \gamma)A_i + \theta\right]\dot{x}_i ep_i' - \alpha A_i x_i ep_i' + \beta A_i x_i^3 ep_i'\right)\mathrm{d}u_i. \tag{15a}$$

According to the definitions in Eq. (12) and result that $\int_0^{T_i} ep_i'^2 \mathrm{d}u_i \neq 0$ and $\int_0^{T_i} ep_i^m ep_i' \mathrm{d}u_i = 0, \ m \in Z$ [37], Eq. (15a) is reduced to give

$$\dot{A}_i = \varepsilon\theta A_i^2 - (\rho - \gamma)A_i + \theta. \tag{15b}$$

Since A_i slowly varies, it is taken that $\dot{A}_i = 0$ which leads to

$$A_{i1} = \frac{\rho-\gamma-\sqrt{(\rho-\gamma)^2-4\varepsilon\theta^2}}{2\varepsilon\theta};\ A_{i2} = \frac{\rho-\gamma+\sqrt{(\rho-\gamma)^2-4\varepsilon\theta^2}}{2\varepsilon\theta} \tag{16}$$

Based on Eq. (16), A_i is defined identically for both intrawell and snap-through vibrations. Moreover, according to Eq. (15), an assessment of stability indicates that the smaller of the two roots in Eq. (16) is the stable root. Then, the voltage is expressed by

$$v_i = \frac{\rho-\gamma-\sqrt{(\rho-\gamma)^2-4\varepsilon\theta^2}}{2\varepsilon\theta}\dot{x}_i \tag{17}$$

To meet the assumptions inherent in the derived form of voltage in Eq. (17), it is apparent that $(\rho-\gamma)^2 \geq 4\varepsilon\theta^2$, which indicates that either the time constant must be large ($\rho \gg 1$) or the electromechanical coupling small ($\theta \ll 1$). In either event, the contexts described above for which it is appropriate to assume that the influence of the electromechanical components is a dissipative effect correspond directly to such assumptions [41].

4.2. Deriving averaged governing equations

This section estimates the displacement amplitude M_i using the averaging method so as to facilitate the subsequent determination of the relevant dynamical variables and time-varying parameters. Substituting Eq. (17) into (3), the original electromechanically-coupled governing equation system is simplified to a conventional Duffing equation

$$\ddot{x}+\gamma_1\dot{x}-\alpha x+\beta x^3 = 0,\ \ x|_{t=0} = x_0,\ \ \dot{x}|_{t=0} = \dot{x}_0 \tag{18}$$

where $\gamma_1 = \gamma + \left(\rho-\gamma-\sqrt{(\rho-\gamma)^2-4\varepsilon\theta^2}\right)/2$. From Eq. (12a), the first order derivatives of x_i is

$$\dot{x}_i = \zeta_i\frac{\mathrm{d}M_i}{\mathrm{d}t}\left[ep_i+\sigma_iM_i\psi_iK_i'k_i'ep_i'+M_ik_i'\frac{\partial ep_i}{\partial k_i}\right]+\zeta_i\frac{\mathrm{d}\psi_i}{\mathrm{d}t}\sigma_iM_iK_iep_i' \tag{19}$$

where $(\cdot)'$ denotes the differentiation of the variables with respect to their respective argument. In other words

$$ep_i' \equiv \partial ep_i/\partial u_i;\ K_i' \equiv \mathrm{d}K_i/\mathrm{d}k_i;\ k_i' \equiv \mathrm{d}k_i/\mathrm{d}M_i;\ \omega_i' \equiv \mathrm{d}\omega_i/\mathrm{d}M_i \tag{20}$$

Comparing Eqs. (12b) and (19) one finds

$$\frac{\mathrm{d}M_i}{\mathrm{d}t}\left[ep_i+\sigma_iM_i\psi_iK_i'k_i'ep_i'+M_ik_i'\frac{\partial ep_i}{\partial k_i}\right]+\frac{\mathrm{d}\psi_i}{\mathrm{d}t}\sigma_iM_iK_iep_i' = M_i\omega_iep_i' \tag{21}$$

From Eq. (12b), the second order derivative of x_i is

$$\ddot{x}_j = \zeta_i\left\{\frac{\mathrm{d}M_i}{\mathrm{d}t}\left[(\omega_i+M_i\omega_i')ep_i'+\sigma_iM_i\psi_i\omega_iK_i'k_i'ep_i''+M_i\omega_ik_i'\frac{\partial ep_i'}{\partial k_i}\right]+\frac{\mathrm{d}\psi_i}{\mathrm{d}t}\sigma_iM_i\omega_iK_iep_i''\right\} \tag{22}$$

Substituting Eqs. (12) and (22) into (18) one obtains

$$\frac{\mathrm{d}M_i}{\mathrm{d}t}\left[(\omega_i+M_i\omega_i')ep_i'+\sigma_iM_i\psi_i\omega_iK_i'k_i'ep_i''+M_i\omega_ik_i'\frac{\partial ep_i'}{\partial k_i}\right]+\frac{\mathrm{d}\psi_i}{\mathrm{d}t}\sigma_iM_i\omega_iK_iep_i''+\gamma_1M_i\omega_iep_i'-\alpha M_iep_i+\beta M_i^3ep_i^3 = 0 \tag{23}$$

Combining Eqs. (21) and (23), $\mathrm{d}M_i/\mathrm{d}t$ and $\mathrm{d}\psi_i/\mathrm{d}t$ are solved using the identities of Jacobian elliptic functions. For intrawell vibration,

$$\mathrm{d}M_d/\mathrm{d}t = -\gamma_1M_d\mathrm{d}n_d'^2/k_d^2 \tag{24a}$$

$$\frac{\mathrm{d}\psi_d}{\mathrm{d}t} = \frac{\omega_d}{2K_d}+\frac{\gamma_1\mathrm{d}n_d'}{2K_dk_d^2}\left\{\mathrm{d}n_d-\frac{2-k_d^2}{k_d^2\left(1-k_d^2\right)}\left[Z(u_d,k_d)\mathrm{d}n_d'+\mathrm{d}n_d\left(1-\mathrm{d}n_d^2\right)\right]\right\} \tag{24b}$$

For snap-through vibration,

$$\mathrm{d}M_c/\mathrm{d}t = -\gamma_1M_ccn_c'^2 \tag{25a}$$

$$\frac{\mathrm{d}\psi_c}{\mathrm{d}t} = \frac{\omega_c}{4K_c}+\frac{\gamma_1cn_c'}{4K_c}\left[cn_c-\frac{1-2k_c^2}{1-k_c^2}\left(Z(u_c,k_c)cn_c'+k_c^2cn_c\left(1-cn_c^2\right)\right)\right] \tag{25b}$$

$Z(u_i,k_i)$ is the Jacobian Zeta function and is hereafter expressed simply by Z_i, $i=c,d$. According to the assumption that the amplitude $M_i = M_i(t)$ and argument $u_i = T_i\psi_i(t)$ slowly vary in time, the averaging method is applied to Eqs. (24a) and (25a) over one cycle of the transient oscillations. Eq. (26a) is the averaged result for intrawell oscillations while Eq. (26b) results

for snap-through vibrations.

$$\dot{M}_d = -\gamma_1 M_d \left[\frac{2\left(k_d^2 - 1\right)}{3k_d^2} + \frac{2-k_d^2}{3k_d^2} \cdot \frac{E_d}{K_d} \right] \tag{26a}$$

$$\dot{M}_c = -\gamma_1 M_c \left[\frac{1-k_c^2}{3k_c^2} + \frac{2k_c^2 - 1}{3k_c^2} \frac{E_c}{K_c} \right] \tag{26b}$$

where the amplitudes M_i are understood to be averaged instantaneous representations of the exact dynamics, and where K_i and E_i denote the complete elliptic integrals of the first and second kinds with respect to the modulus k_i.

4.3. Approximating the functional dependence of the averaged equations

Eqs. (26) are non-integrable and the right hand sides are implicit functions of M_i, which indicates that an alternative means is needed to solve Eqs. (26). The means developed here is to first express Eqs. (26) using

$$\dot{M}_i = -\gamma_1 M_i f_i\left(k_i^2\right), \quad i = c, d \tag{27a}$$

$$f_c\left(k_c^2\right) = \frac{1-k_c^2}{3k_c^2} + \frac{2k_c^2 - 1}{3k_c^2} \cdot \frac{E_c}{K_c}; \; f_d\left(k_d^2\right) = \frac{2\left(k_d^2 - 1\right)}{3k_d^2} + \frac{2-k_d^2}{3k_d^2} \cdot \frac{E_d}{K_d} \tag{27b}$$

It is seen that $f_i\left(k_i^2\right)$ depends only on k_i^2, which itself can be expressed in terms of a new variable defined by $\alpha/\beta M_i^2$ by way of the relations in Eqs. (6) and (7). As a result, one finds

$$k_d^2 = 2 - 2\alpha/\left(\beta M_d^2\right); \quad 1/2 \le \alpha/\beta M_d^2 \le 1 \tag{28a}$$

$$k_c^2 = 1/\left[2\left(1 - \alpha/\beta M_c^2\right)\right]; \quad 0 \le \alpha/\beta M_c^2 \le 1/2 \tag{28b}$$

Eq. (28) provides the connection between the new variable $\alpha/\beta M_i^2$ and the function $f_i\left(k_i^2\right)$. Across the range of validity of these expressions, it is found that both $f_d\left(k_d^2\right)$ and $f_c\left(k_c^2\right)$ are sufficiently smooth on a large range of the respective variables $\alpha/\beta M_i^2$. Consequently, a second-order polynomial approximation is utilized to reconstruct the curvilinear dependence of $f_i\left(k_i^2\right)$ on $\alpha/\beta M_i^2$. The MATLAB curve-fitting toolbox is employed to this end. For intrawell oscillations, the polynomial fit is taken across the range $0.55 \le \alpha/\beta M_d^2 \le 1$ which is found to be most amenable to fitting. Then,

$$f_d\left(k_d^2\right) \approx g_d = \mu \cdot \left(\frac{\alpha}{\beta M_d^2} \right)^{n_d} + \upsilon \tag{29}$$

where $n_d = 2$ is the order, and $\mu = -0.15011$ and $\upsilon = 0.14714$ are fitting coefficients, which yield a goodness-of-fit measure of $R^2 = 0.9987$ across $0.55 \le \alpha/\beta M_d^2 \le 1$. Similarly, the suitable range for a second-order polynomial fit for individual polynomial fit using $f_c\left(k_c^2\right)$ is found to be $0.05 \le \alpha/\beta M_c^2 \le 0.45$. The function fit results in

$$f_c\left(k_c^2\right) \approx g_c = a \cdot \left(\frac{\alpha}{\beta M_c^2} \right)^{n_c} + b \tag{30}$$

where $n_c = 2$, $a = -0.785783$, and $b = 0.320508$ which yields $R^2 = 0.9962$. The functions g_i given in Eqs. (29) and (30) provide the alternative means to integrate Eqs. (26), with best fitting accuracy – and thus anticipated accuracy of analytical predictions – across the range of $\alpha/\beta M_i^2$ for which the fits are obtained.

Substitution of g_i into the appropriate form of Eq. (27), and integration of the equation provides for the analytical prediction of the time-varying displacement amplitude as a function of system parameters and fitting coefficients. For intrawell oscillations

$$M_d(t) = \beta^{-1/2} \cdot \left[\left(\frac{\mu}{\upsilon}\alpha^2 + \beta^2 M_{d0}^4 \right) e^{-4\upsilon\gamma t} - \frac{\mu}{\upsilon}\alpha^2 \right]^{1/4} \tag{31}$$

in which M_{d0} is the initial amplitude determined from Eq. (10a). For snap-through vibrations

$$M_c(t) = \beta^{-1/2} \cdot \left[\left(\beta^2 M_{c0}^4 + \frac{a}{b}\alpha^2 \right) e^{-4b\gamma_1 t} - \frac{a}{b}\alpha^2 \right]^{1/4} \tag{32}$$

where M_{c0} is the initial amplitude likewise determined using Eq. (10a). Considering the criteria which demarcates intrawell from snap-through behaviors, $\beta M_i^2 = 2\alpha$, the time at which the analytical predictions of decaying snap-through vibrations

cease to meet constraints is

$$t_{end} = -\ln\left[(4+a/b)\alpha^2\cdot\left(\beta^2 M_{c0}^4+\alpha^2 a/b\right)^{-1}\right]/4b\gamma_1 \tag{33}$$

Eqs. (31) and (32) are analytical approximations of the averaged instantaneous displacement amplitude, more often described to be "envelopes" of the response. Although this information is sufficient with which to predict the instantaneous converted electrical power and net converted energy, this research follows through on a fuller analytical development for the prediction of time-dependent trajectories of the electromechanical dynamics, including the instantaneous frequency spectrum.

4.4. Prediction of the instantaneous spectral information

The transient, nonlinear vibrations of the harvester possess time-varying response amplitudes that correspond to changing spectral components. The transient frequency information is thus found in this subsection. Based upon the assumptions described at the outset of Section 4, the arguments of the Jacobian elliptic functions, and hence frequencies, are slowly varying in time. To predict the transient electromechanical dynamics of displacement x_i and voltage v_i, the time dependence of the frequencies must be determined in addition to the transient amplitudes as derived in Eqs. (31) and (32).

For intrawell oscillations, the averaged instantaneous variable $\dot{\bar{\psi}}_d$ is found by averaging Eq. (24b) over one vibration period $2K_d$.

$$\dot{\bar{\psi}}_d = \frac{\omega_d}{2K_d}+\frac{1}{2K_d}\int_0^{2K_d}\frac{\gamma_1}{2K_d k_d^2}\left\{\mathrm{d}n'\left[\mathrm{d}n-\frac{2-k_d^2}{k_d^2\left(1-k_d^2\right)}\cdot\mathrm{d}n\left(1-\mathrm{d}n^2\right)\right]-\frac{2-k_d^2}{k_d^2\left(1-k_d^2\right)}Z_d\mathrm{d}n'^2\right\}\mathrm{d}u_d \tag{34}$$

which simplifies to $\dot{\bar{\psi}}_d = \omega_d/2K_d$ following application of the identity $\int_0^{2K_d} Z_d \mathrm{d}n^s \mathrm{d}u_d = 0,\ s = 0,1,2,\ldots$ [37]. Note that the Jacobian elliptic function dn is able to be expressed by the Fourier series

$$dn(u_d,k_d) = \frac{\pi}{2K_d}+\frac{2\pi}{K_d}\sum_{j\,=\,1,2,3,\ldots}^{\infty}\frac{q_d^j}{1+q_d^{2j}}\cos\left(\frac{j\pi}{K_d}u_d\right),\ j=1,2,3,\ldots \tag{35}$$

Eq. (35) reveals that intrawell oscillations are composed of even- and odd-order harmonic components, a finding in agreement with established understanding on their spectral dependence [42]. The angular frequencies of the intrawell vibration are

$$\Omega_{dj} = \frac{d}{dt}\left(\frac{j\pi}{K_d}u_d\right) = \frac{d}{dt}\left(\frac{j\pi}{K_d}T_d\psi_d(t)\right),\quad j=1,2,3,\ldots \tag{36}$$

where j indicates the order of harmonic components; $q_d = e^{-\pi K_d'/K_d}$; $K_d' = K(l_d)$; and $l_d = \sqrt{1-k_d^2}$. The averaged instantaneous frequencies are therefore

$$\bar{\Omega}_{dj} = \frac{1}{2K_d}\int_0^{2K_d}\frac{d}{dt}\left(\frac{j\pi}{K_d}\cdot 2K_d\psi_d\right)\mathrm{d}u_d = \frac{1}{2K_d}\int_0^{2K_d} 2j\pi\dot{\psi}_d\mathrm{d}u_d = 2j\pi\cdot\frac{\omega_d}{2K_d} = \frac{j\pi\omega_d}{K_d} \tag{37a}$$

To distinguish Ω_{dj} and ω_d, the prior corresponds to the lowest-order frequency of the dissipative and coupled vibration when $j=1$ while, as described in Section 3, ω_d is the lowest-order oscillation frequency for the undamped and uncoupled system. Then, recalling $x_d = \zeta_d M_d \mathrm{d}n$ and Eq. (35), the amplitudes of the bistable harvester displacement corresponding to the frequency components are

$$Y_{dj} = M_d\mathrm{d}n|_{\Omega_{dj}} = M_d\cdot\frac{2\pi}{K_d}\cdot\frac{q_d^j}{1+q_d^{2j}} = \frac{2\pi M_d}{K_d}\cdot\frac{q_d^j}{1+q_d^{2j}},\quad j=1,2,3,\ldots \tag{37b}$$

A comparable routine is undertaken to determine the transient spectral features in the context of snap-through vibrations. In this event, the averaged instantaneous variable $\bar{\psi}_c$ is derived by averaging Eq. (25b) over one period $4K_c$

$$\dot{\bar{\psi}}_c = \frac{\omega_c}{4K_c}+\frac{1}{4K_c}\int_0^{4K_c}\frac{\gamma_1 cn'}{4K_c}\left[cn-\frac{1-2k_c^2}{1-k_c^2}\cdot k_c^2 cn\left(1-cn^2\right)\right]\mathrm{d}u_c-\frac{1}{4K_c}\int_0^{4K_c}\frac{\gamma_1}{4K_c}\cdot\frac{1-2k_c^2}{1-k_c^2}\cdot Z_c\left(1-cn^2\right)\left(1-k_c^2+k_c^2cn^2\right)\mathrm{d}u_c \tag{38}$$

which reduces similarly to $\dot{\bar{\psi}}_c = \omega_c/4K_c$. The Jacobian elliptic function cn may be expanded in the following Fourier series

$$cn(u_c,k_c) = \frac{2\pi}{k_c K_c}\sum_{i\,=\,1,3,5,\ldots}^{\infty}\frac{q_c^i}{1+q_c^{2i}}\cos\left(\frac{i\pi}{K_c}u_c\right) \tag{39}$$

where $q_c = e^{-\pi K_c'/K_c}$; $K_c' = K(l_c)$; and $l_c = \sqrt{1-k_c^2}$ is the complementary modulus. Eq. (39) reveals that snap-through vibration contains only the odd-order harmonic components, also in agreement with previous understood properties of bistable

structures [35]. Then the angular frequency of each harmonic component is expressed as

$$\Omega_{c,i}=\frac{\mathrm{d}}{\mathrm{d}t}\left(\frac{i\pi}{K_c}u_c\right),\quad i=1,3,5,\ldots \tag{40}$$

The averaged instantaneous angular frequency is thus

$$\overline{\Omega}_{c,i}=\frac{1}{4K_c}\int_0^{4K_c}\frac{\mathrm{d}}{\mathrm{d}t}\left(\frac{i\pi}{K_c}\cdot 4K_c\psi_c\right)\mathrm{d}u_c=\frac{i\pi\omega_c}{K_c},\quad i=1,3,5,\ldots \tag{41}$$

Combining Eqs. (12a) and (39), the amplitude of displacement corresponding to each harmonic component is

$$Y_{c,i}=M_c cn|_{\Omega_{c,i}}=M_c\cdot\frac{2\pi}{k_cK_c}\cdot\frac{q_c^i}{1+q_c^{2i}}=\frac{2\pi M_c}{k_cK_c}\cdot\frac{q_c^i}{1+q_c^{2i}},\quad i=1,3,5,\ldots \tag{42}$$

4.5. Prediction of the instantaneous trajectories of response

With the time-varying spectral information available, the instantaneous trajectories of the displacement, velocity, and voltage may be determined. The instantaneous displacement and velocity are given according to Eq. (12). To reconstruct the trajectories in time, the transient argument $u_i=\sigma_iK_i\psi_i$ of the Jacobian elliptic function ep_i must be approximated. The derivative of the argument u_i is

$$\dot{u}_i=\frac{d}{dt}(\sigma_iK_i\psi_i)=\sigma_i\psi_iK_i'k_i'\dot{M}_i+\sigma_iK_i\dot{\psi}_i \tag{43}$$

Then the definition of K_i' and derivative of k_i' are expressed as

$$K_i'\equiv\mathrm{d}K_i/\mathrm{d}k_i=\left(E_i/l_i^2-K_i\right)/k_i;\ k_c'\equiv\mathrm{d}k_c/\mathrm{d}M_c=-\left(2k_c^2-1\right)\cdot k_c/M_c;\ k_d'\equiv\mathrm{d}k_d/\mathrm{d}M_d=\left(2-k_d^2\right)/(k_dM_d) \tag{44}$$

For intrawell vibration, substituting Eq. (27) into (43) one obtains

$$\dot{u}_d=-2\gamma_1\psi_d\left(\frac{E_d}{l_d^2}-K_d\right)\cdot\frac{2-k_d^2}{k_d^2}\cdot\left(\frac{E_d}{l_d^2}-K_d\right)\left[\frac{2\left(k_d^2-1\right)}{3k_d^2}+\frac{2-k_d^2}{3k_d^2}\frac{E_d}{K_d}\right]+2K_d\dot{\psi}_d \tag{45}$$

Substituting Eq. (31) into Eq. (43) and subsequently substituting the result into Eq. (45), the averaged instantaneous argument $\dot{\bar{u}}_d$ is

$$\dot{u}_d=-2\gamma_1\psi_d\left(\frac{E_d}{l_d^2}-K_d\right)\cdot\frac{2-k_d^2}{k_d^2}\cdot\left(\frac{E_d}{l_d^2}-K_d\right)\left[\frac{2\left(k_d^2-1\right)}{3k_d^2}+\frac{2-k_d^2}{3k_d^2}\frac{E_d}{K_d}\right]+\omega_d \tag{46}$$

Using the initial values defined in Section 4, $\psi_d(t)$ and $u_d(t)$ are approximated on any time interval $[0,t]$ by integrating Eqs. (34) and (46)

$$\psi_d(t)=\psi_d(0)+\int_0^t\dot{\psi}_d\mathrm{d}t\cong\frac{\varphi_{d0}}{2K_d}+\int_0^t\bar{\dot{\psi}}_d\mathrm{d}t=\frac{\varphi_{d0}}{2K_d}+\int_0^t\frac{\omega_d}{2K_d}\mathrm{d}t \tag{47a}$$

$$u_d(t)=u_d(0)+\int_0^t u^d\mathrm{d}t\cong\varphi_{d0}+\int_0^t\left\{-2\gamma\psi_d\frac{2-k_d^2}{k_d^2}\left(\frac{E_d}{l_d^2}-K_d\right)\left(\frac{2\left(k_d^2-1\right)}{3k_d^2}+\frac{2-k_d^2}{3k_d^2}\frac{E_d}{K_d}\right)+\omega_d\right\}\mathrm{d}t. \tag{47b}$$

Using the same approach in the context of snap-through vibrations, Eqs. (32) and (44) are substituted into (43) to yield

$$\dot{u}_c=4\gamma_1\psi_c\left(\frac{E_c}{l_c^2}-K_c\right)\left(2k_c^2-1\right)\left[a\left(\frac{\alpha}{\beta C^2}\right)^2+b\right]+4K_c\dot{\psi}_c. \tag{48}$$

The averaged instantaneous $\dot{\bar{u}}_c$ is therefore

$$\dot{\bar{u}}_c=4\gamma_1\psi_c\left(\frac{E_c}{l_c^2}-K_c\right)\left(2k_c^2-1\right)\left[a\left(\frac{\alpha}{\beta M_c^2}\right)^2+b\right]+\omega_c. \tag{49}$$

Using the respective initial values, $\psi_c(t)$ and $u_c(t)$ are determined to be

$$\psi_c(t)=\psi_c(0)+\int_0^t\bar{\dot{\psi}}_c\mathrm{d}t\cong\frac{\varphi_{c0}}{4K_c}+\int_0^t\bar{\dot{\psi}}_c\mathrm{d}t=\frac{\varphi_{c0}}{4K_c}+\int_0^t\frac{\omega_c}{4K_c}\mathrm{d}t \tag{50a}$$

$$u_c(t)=u_c(0)+\int_0^t\dot{u}_c\mathrm{d}t\cong\varphi_{c0}+\int_0^t\left\{4\gamma_1\psi_c\left(\frac{E_c}{l_c^2}-K_c\right)\left(2k_c^2-1\right)\left[a\left(\frac{\alpha}{\beta M_c^2}\right)^2+b\right]+\omega_c\right\}\mathrm{d}t \tag{50b}$$

Using Eqs. (47b) and (31) with Eq. (12), the displacement and velocity of the bistable harvester in the intrawell oscillation regime may be reconstructed. For snap-through vibrations, Eqs. (50b) and (32) with Eq. (12) provide the corresponding time-dependent trajectories. In both cases, Eq. (17) gives the link to the resulting transduced voltage in time. While the predicted *amplitudes* of displacement, velocity, and voltage are analytical in nature, the prediction of the time-varying trajectories of these responses is effectively both analytical and numerical according to Eqs. (47b) and (50b). In other words, performance measures of the energy harvester tied strictly to the response amplitudes may be predicted analytically using less computational expense than performance measures which require the full trajectories to be reconstructed.

4.6. Prediction of the instantaneous electrical power and net converted energy

Using the estimated dynamic response amplitudes, the instantaneous harvested power is evaluated in this subsection. Recalling Eq. (17), the instantaneous power generated by the bistable energy harvester is thus

$$p_i(t) = v_i^2/R = \left[\left(\rho-\gamma-\sqrt{(\rho-\gamma)^2-4\varepsilon\theta^2}\right)\Big/(2\varepsilon\theta)\right]^2 \cdot M_i^2 \cdot \omega_i^2 \cdot ep_i'^2/R, \quad i=c,d \tag{51}$$

Then, the averaged instantaneous powers over one period of intrawell or snap-through oscillation are found, respectively, to be

$$\overline{p}_d(t) = \frac{\left[\left(\rho-\gamma-\sqrt{(\rho-\gamma)^2-4\varepsilon\theta^2}\right)\Big/(2\varepsilon\theta)\right]^2 \cdot \beta M_d^4}{2R} \cdot \left[\frac{2\left(k_d^2-1\right)}{3}+\frac{2-k_d^2}{3}\frac{E_d}{K_d}\right] \tag{52b}$$

$$\overline{p}_c(t) = \frac{\left[\left(\rho-\gamma-\sqrt{(\rho-\gamma)^2-4\varepsilon\theta^2}\right)\Big/(2\varepsilon\theta)\right]^2 \cdot M_c^2 \cdot \left(\beta M_c^2-\alpha\right)}{R} \cdot \left[\frac{1-k_c^2}{3k_c^2}+\frac{2k_c^2-1}{3k_c^2}\frac{E_c}{K_c}\right] \tag{52a}$$

By Eq. (52), it is evident that the averaged, instantaneous power per cycle $\overline{p}_i$ diminishes over time according to the expressions for M_i. The net converted energy over a given time interval $[0, t]$ is

$$\overline{e}_i(t) = \int_0^t \overline{p}_i(\tau)\mathrm{d}\tau \tag{53}$$

While average power is a common measure of performance in examinations of persistently excited vibration energy harvesting systems, its meaning is less effective when the dynamic behaviors are impulsive and decaying in nature. Thus, the more meaningful measure employed here is the net energy converted over a prescribed time interval, Eq. (53).

5. Experimental system overview

The parameters utilized throughout the following analytical and numerical studies correspond to the experimental system explored in this research. A bistable piezoelectric cantilever is considered, Fig. 2, where the design is similar to that

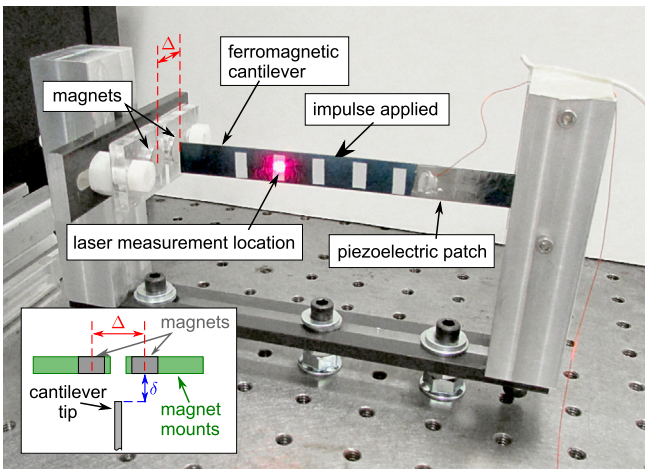

Fig. 2. Bistable piezoelectric cantilever with bistability induced due to the combination of elastic effects in the ferromagnetic beam and two magnets positioned near to the beam tip and separated by distance Δ mm. Impulses are applied approximately at the beam position oppositely measured by the laser interferometer.

illustrated in Fig. 1. The spring steel cantilever (length 125 mm, width 12.7 mm, thickness 0.508 mm) is ferromagnetic, and bistability is induced due to the combination of elastic and magnetic forces exerted at the beam tip. Thus, the primary generalized displacement is the beam tip motion [43]. The magnets are spaced apart from each other, center-to-center, by a distance Δ mm, while they are spaced approximately $\delta = 6.84$ mm away from the cantilever tip, in the manner shown in the inset of Fig. 2. A piezoelectric patch (Piezo Systems T110-A4E-602) of length 11.8 mm and width 12.7 mm is bonded to one side of the beam surface using silver epoxy (MG Chemicals 8331) such that the patch is spaced from the cantilevered end by 19.8 mm. The asymmetric elastic influences of the bonded piezoelectric patch are found to be negligibly small in comparison to the effects induced by the magnets and are thus neglected in the following. According to the governing Eq. (1), Table 1 presents the relevant system parameters that are identified via measurements (e.g., the damping constant by the log-decrement method, or capacitance by multi-meter readout) or textbook relations (e.g., the equivalent mass of a cantilevered beam from Ref. [44]). Measurements during experimentation are acquired of the beam displacement and velocity using a laser interferometer (Polytec OFV-534, OFV-5000) and of the transduced voltage across the load resistance R. Data is collected via National Instruments hardware through a LabVIEW software interface. To apply impulses experimentally, following an extensive evaluation of possible approaches it is seen that manual impacts by fingertip are the most repeatable method. Moreover, with such impulses applied at the beam surface opposite that of the laser spot, this method is found to minimize the possibility for multi-mode dynamics which would lead to discrepancies with the analytical and simulation results that account for only one generalized displacement. The laser spot location was approximately positioned at two-thirds of the beam length from the cantilevered end, such as that shown in Fig. 2.

6. Numerical validation of the analytical formulation

The fidelity of the analytical prediction approach developed here is best assessed in relation to the "exact" dynamics of the system resulting from an impulsive excitation. The best comparison is therefore the direct simulation of the governing Eq. (1), which is hereby considered to be "exact". For the numerical integration of the Eq. (1), a tight tolerance is required from the fourth-order Runge–Kutta algorithm to ensure that such exactness is obtained in simulation. Using the parameters of the experimental system given in Table 1, the comparison of analytical and numerical results are taken across a substantial range of initial velocities, representative of a wide range of impulse strengths. Fig. 3 shows two representative cases in which the initial displacement of the cantilever is at $x_0 = \sqrt{k_1/k_3}$ m at the time of impulse, $t = 0$ s. In Fig. 3(a,b), results are shown of the displacement and power, respectively, for an impulse-imposed initial velocity $\dot{x}_0 = 0.2935$ m/s, while (c,d) show corresponding results for the initial velocity $\dot{x}_0 = 0.2225$ m/s. The solid curves denote the numerical simulation trajectories, dotted curves correspond to analytically-predicted instantaneous averaged quantities, and dashed curves correspond to the analytically-reconstructed trajectories.

Considering the instantaneous averaged quantities (dotted curves) in Fig. 3(a and c), it is apparent that the analytically predicted displacement amplitudes correctly track the envelopes of the numerical trajectories. The instantaneous averaged powers in Fig. 3(b,d) likewise capture the mean behavior of the numerical power trajectories. In the case shown in Fig. 3(b), a small, positive relative error (+ 0.290%) in the net converted energy during the snap-through oscillations is produced for the initial velocity $\dot{x} = 0.2935$ m/s, while a more substantial underprediction of the power generation (−6.50%) is given by the analysis when the initial velocity is smaller, $\dot{x} = 0.2225$ m/s, as shown in Fig. 3(d). Indeed, in the limiting case that the initial velocity is at the threshold of activating snap-through oscillations according to the criterion given in Section 3, the error of the net converted energy for this dynamic regime increases to larger negative values, Fig. 3(a). This is because in the limiting case that the initial velocities are gradually reduced so that snap-through behaviors are barely triggered, this corresponds to the trend that $\alpha/\left(\beta M_{c0}^2\right) \to 1/2$ which is beyond the range for which the polynomial fit of the function $f_c\left(k_c^2 \Leftrightarrow \alpha/\beta M_c^2\right)$ is made.

In terms of the instantaneous displacement trajectories predicted by the analysis, dashed curves in Fig. 3(a,c), excellent agreement with the numerical results is obtained for the snap-through vibration regime. For the analysis, this prediction ceases at the time when the constraint on $\alpha/\beta M_c^2(t)$ is crossed. At the time just prior to the end of the snap-through dynamics analytical prediction, identified in Fig. 3 as the point in time where the corresponding amplitude prediction ceases, the integrand argument in Eq. (50b) increases asymptotically. Based upon the exact time resolution (or time step) at which the analytical trajectories are generated, this asymptotic trend may lead to a sudden jump in the trajectories prediction. Both of the cases in Fig. 3(a) and (c) show such a jump in the displacement due to high resolution of time series employed. The values of the numerical simulations which correspond to the final prediction time for the analytical snap-through trajectories are

Table 1
Experimental system parameters used throughout all following analyses and numerical simulations.

Mass, m [g]	Damping, d [N.s/m]	Stiffness, k_1 [N/m]	Stiffness, k_3 [N/m^3]
1.48	6.76×10^{-3}	10.2	1.16×10^{6}
Piezoelectric coupling, Γ [N/V]	Capacitance, C_p [F]	Resistance, R [Ohm]	
0.0422×10^{-3}	8.00×10^{-9}	99.5×10^{3}	

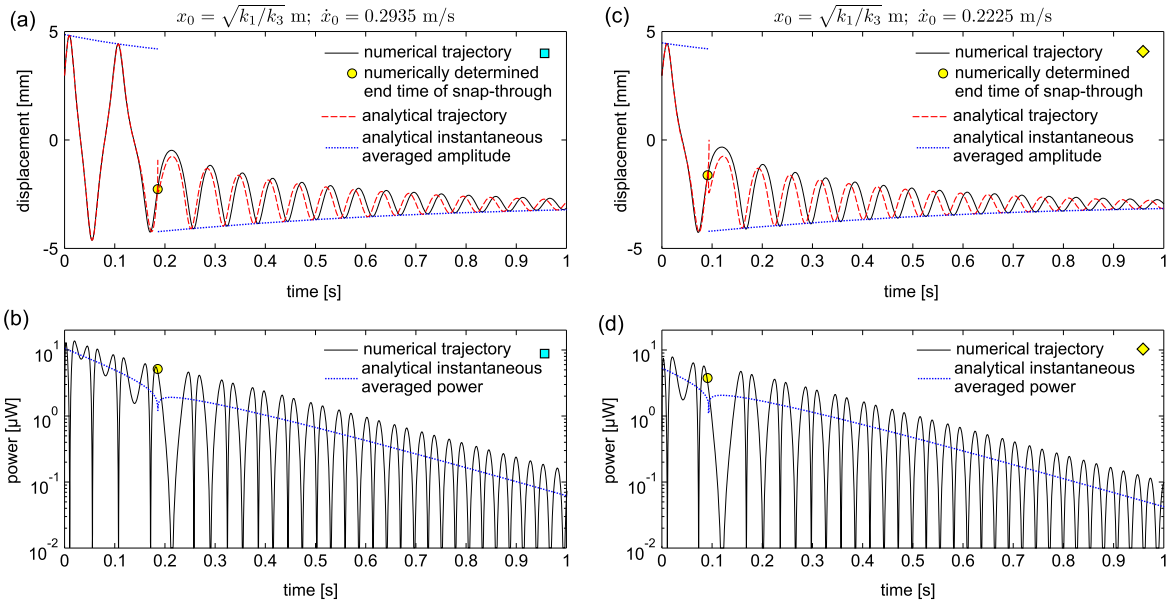

Fig. 3. Comparison of numerical simulation results with analytical predictions. In all sub-figs, the initial displacements of the assessments are taken as the positive stable equilibria. In (a,b) the initial velocity is $\dot{x} = 0.2935$ m/s, while in (c,d) the initial velocity is $\dot{x} = 0.2225$ m/s. In (a,c) are shown the displacement trajectories while in (b,d) are shown the corresponding electrical powers across the load resistance. In (b) the analytical estimation of the net converted energy during snap-through is 1.038 μJ while the numerical counterpart is 1.035 μJ. In (d) the analytical estimation of the net converted energy during snap-through is 0.3296 μJ while the numerical counterpart is 0.3525 μJ.

then employed as initial values for the analysis, at which point the analytical formulation predicts the resulting *intrawell* oscillations that occur in the final'ring-down' phase of the impulse-excited dynamics. The instantaneous trajectories as predicted by the analysis are in good agreement overall but have a noticeable phase error. This phase error results because the intrawell predictions likewise begin in a regime of the parameter $\alpha/\beta M_{d0}^2$ outside of which the polynomial fit is made for the function $f_d\left(k_d^2 \Leftrightarrow \alpha/\beta M_d^2\right)$. Such phase error is not seen if the initial velocities are well within the constraints for the intrawell dynamic regime. On the other hand, this latter case corresponds to a weakly nonlinear, decaying oscillation which is suitably predicted using a variety of analytical predictions strategies [26,28,24], not simply the new analytical approach devised here.

Finally, Fig. 4(a) shows that for larger initial velocities (greater impulse strengths), the relative error of the net converted energy predictions for snap-through vibrations becomes relatively convergent to approximately 2% of overprediction with respect to the numerical simulation findings. The example in Fig. 4(b) indicates why this trend occurs. It is seen that the analytical voltage trajectory begins with a finite value which is not the case for the simulated trajectory. Based upon the voltage relation defined in Eq. (17), the proportionality of voltage to velocity (which is finite at the initial time) indicates that there will be an error in the net converted energy at early times. Of course, for increasing initial velocities, such *absolute* error will grow. On the other hand, the overall time span of snap-through dynamics increases for larger initial velocities, and across the long-time span of evaluation there is excellent agreement between the analytical predictions of voltage and the numerical results. These two effects counterbalance each other, such that the progressively increasing absolute error at early times is offset by an overall accurate prediction for the increasing times of evaluation. Thus, the *relative* error obtains a convergent-like property as shown in Fig. 4(a) for larger initial velocities.

The results of Figs. 3 and 4 reveal that the analytical approach created in this research leads to faithful reconstruction of the time-varying response amplitudes determined through numerical simulations. Moreover, the analytical predictions of the net converted energy during the snap-through regime – the more desirable energy harvesting dynamic, as evident in Fig. 1 – lead to an overall good agreement with simulations as shown in Fig. 4(a). Yet to fully validate the benefit of this new analytical tool, a rigorous experimental study is undertaken.

7. Experimental validation of the analytical formulation

To put the analytical approach to useful practice, the energy conversion predictions must be sufficiently accurate with respect to that seen in experimental systems so as to facilitate the effective development and deployment of bistable energy harvesters in impulsive environments. Additionally, the approach must be accurate across a wide range of operational conditions, namely impulse strengths corresponding to different initial velocities. To lend such comprehensive validation of the analytical tool, a large amount of data is obtained using the experimental system described in Section 5. The experiments are conducted in the shortest possible duration of laboratory time to ensure that testing conditions do not

substantially change during the data acquisition period. Impulses are applied to the cantilever over 1800 times; of this number, over 83% are of sufficient strength to trigger snap-through vibrations for a portion of the overall recording of transient, decaying oscillations. Before beginning a new trial, the vibrations are allowed to decay until the displacement readout approaches the noise threshold. Five different magnet spacing distances Δ, as illustrated in Fig. 2, are employed, each of which produce different values of the stiffnesses k_1 and k_3 [43], and thus different stable equilibria locations and linear natural frequencies, given in Table 2. (The analytical and numerical results of Section 6 are obtained for the parameters k_1 and k_3 corresponding to $\Delta = 37.4$ mm). By carrying out experiments using a wide range of magnet spacing distance, the intent is to assess the robustness of the predictions to important design parameter changes that tailor the bistable harvester dynamic sensitivities. It is seen that the harvester beam tip velocity almost instantaneously increases from a near-stationary state to a large, finite value upon application of the impulse; consequently, the peak, sudden initial velocity resulting from the impulse is determined to be the energy harvester initial velocity value used in the corresponding analytical comparison of a given experiment.

Fig. 5 compares the analytical and experimental results for a case of intrawell oscillations with $\Delta = 37.4$ mm, showing (a) the displacement trajectories in time, (b) the voltage trajectories, and finally (c) the time–frequency distribution of the displacement. This example case is one in which snap-through dynamics occur initially, prior to the intrawell oscillations shown in Fig. 5. Small phase differences between the analytical and experimental findings are evident in Fig. 5(a and b), although the nonlinear oscillations are reconstructed by the analytical approach to an overall high degree of fidelity. The spectral distribution of the displacement response, as plotted in Fig. 5(c), indicates that the lowest three Fourier series components are in very good agreement between measurements and predictions. While the time–frequency analytical predictions are shown directly, the displacement measurements are processed using short-time Fast Fourier transforms (SFFT), and the underlying contour plot presents the result in a decibel scale in reference to a 1 mm amplitude. Due to the SFFT algorithm, not all of the time–frequency features may be extracted, namely at initial and final times where insufficient data is available in the sampling window. For intrawell oscillations, the lowest-order Fourier component is related to the non-zero equilibrium position, and thus leads to a constant Fourier coefficient at zero frequency. The second- and third-order Fourier coefficients

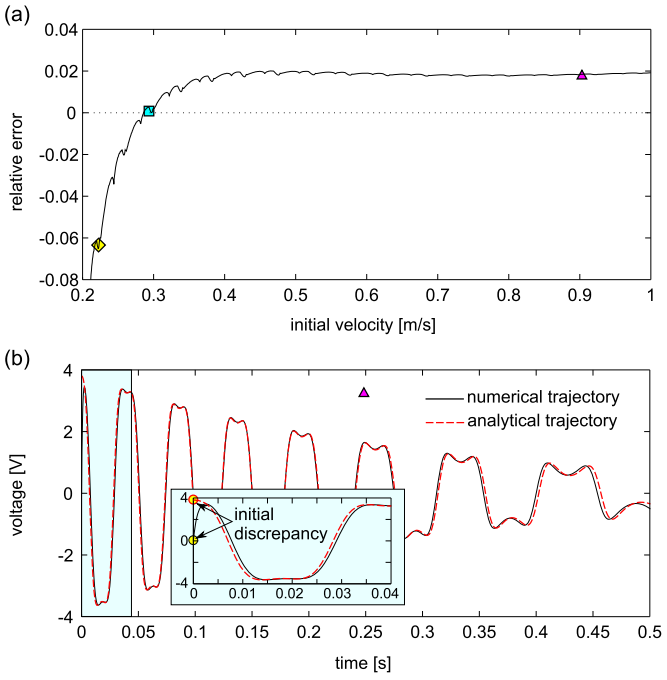

Fig. 4. (a) Relative error between the analytical prediction and simulated result of the net converted energy during snap-through oscillations. The square, diamond, and triangle symbols denote the corresponding example cases given in Fig. 3(a,b), Fig. 3(c,d), and Fig. 4(b), respectively. (b) Comparison of numerical simulation results with analytical predictions for the initial displacement $x_0 = \sqrt{k_1/k_3}$ m and initial velocity of $\dot{x}_0 = 0.903$ m/s. The inset shows the discrepancy in trajectory results at the initial time.

Table 2
Experimental system magnet spacing distances, Δ, and corresponding stable equilibria locations $\sqrt{k_1/k_3}$ and linear natural frequencies $\sqrt{2k_1/m}/2\pi$.

Δ [mm]	35.2	36.2	37.4	38.7	40.0
$\sqrt{k_1/k_3}$ [mm]	1.919	2.490	2.968	3.076	3.100
$\sqrt{2k_1/m}/2\pi$ [Hz]	14.80	17.44	18.70	17.39	13.98

predicted analytically show a gradually increasing trend in time, a feature likewise observed in the post-processed measurement. Such behavior is recognized to be due to the reduced influence of dynamic softening which occurs for larger-amplitude oscillations in bistable structures when confined to one local well of potential energy [45].

The good agreement in the example case of Fig. 5 between the predictions and measurements of both instantaneous trajectories and overall response amplitudes is an indication that the net converted energy during the intrawell oscillation regime is likewise in agreement. In fact, as Fig. 6 shows, for each magnet spacing distance Δ employed in the study, the analytical prediction is found to be an accurate predictor of the converted energy measured across a substantial range of initial velocities. In the plots, the solid curves denote the analytical results while data points are the measurements. In some cases, measurements are obtained using greater initial velocities than the analysis predicts are possible for the intrawell oscillation regime; in other words, the analytical constraint for intrawell oscillation is violated according to the initial velocity at which the corresponding experiment occurs. The most likely source of this discrepancy is the high sensitivity observed in terms of system parameter identification leading to the stiffness coefficients k_1 and k_3 which are identified experimentally using the stable equilibria locations and the local linear natural frequencies. These stiffness coefficients thereafter relate to the coefficients α and β that define the constraint on $\alpha/\beta M_{d0}^2$. Overall, however, the analytical approach accurately predicts the actual converted energy from the impulsive excitation in the intrawell oscillation regime.

As Fig. 1(c) illustrates, the *snap-through dynamics* are much preferred in the utilization of bistable structures for energy harvesting purposes due to the substantially greater energy conversion possible from the large-amplitude vibrations. Thus, for its most productive implementation, the analytical approach must be able to faithfully predict the anticipated energy conversion performance of the snap-through dynamics in the experimental system. Fig. 7 presents one representative case of the time dependence of displacement and voltage snap-through trajectories and the spectral diffusion as predicted analytically and measured in experiment. Overall, there is an exceptionally good agreement between the dynamic behaviors. A particularly accurate reconstruction is generated in the displacement trajectories in time, Fig. 7(a).

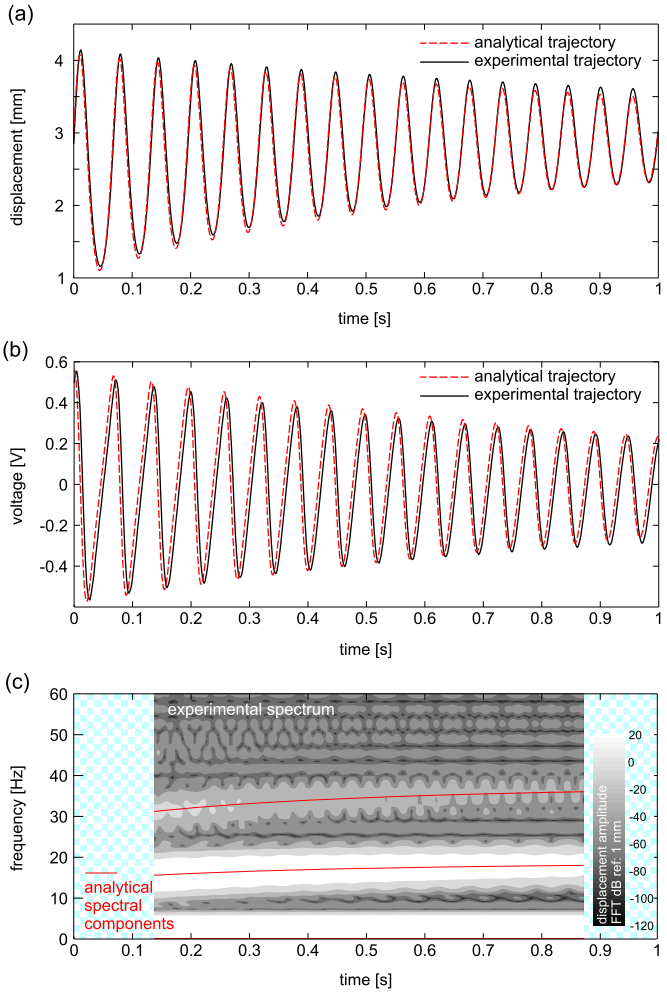

Fig. 5. Comparison of analytically predicted and measured intrawell oscillations following an impulse imposed initial velocity. (a) Displacement trajectories, (b) voltage trajectories, and (c) the time–frequency distribution of the primary spectral components.

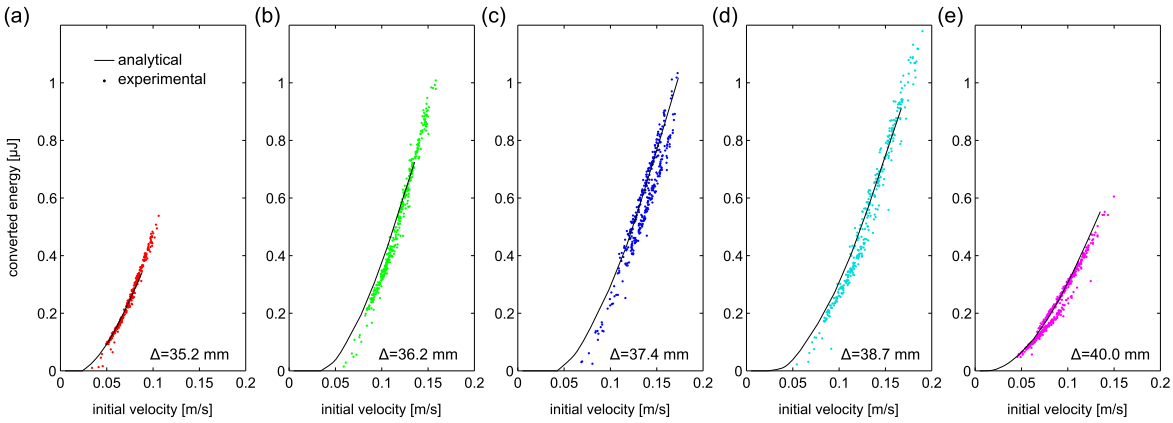

Fig. 6. Comparison of the net converted energies for the intrawell oscillation regime as predicted analytically (curves) and measured experimentally (points). The magnet spacing distance Δ varies from (a) 35.2 mm, (b) 36.2 mm, (c) 37.4 mm, (d) 38.7 mm, and finally to (e) 40.0 mm.

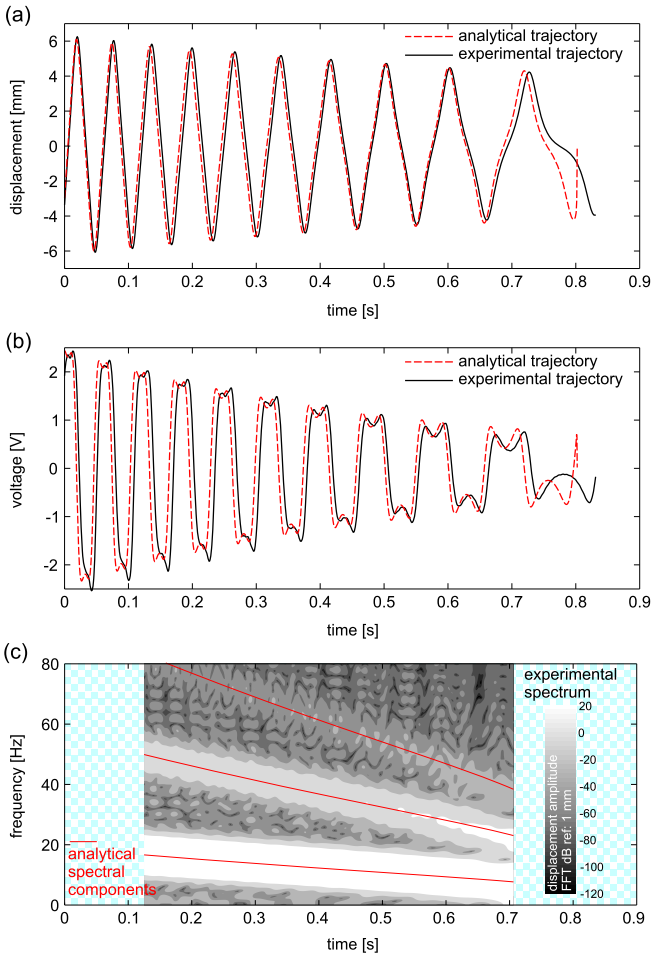

Fig. 7. Comparison of analytically predicted and measured snap-through vibrations following an impulse imposed initial velocity. (a) Displacement trajectories, (b) voltage trajectories, and (c) the time–frequency distribution of the primary spectral components.

The voltage measurements in Fig. 7(b) show evidence of possible multi-mode oscillations or system asymmetry, although the asymmetric-like influences decay in significance over time, which leads to progressively greater agreement with the symmetric oscillations that are analytically predicted. On the other hand, the discrepancy in such symmetry at early times leads to a relative phase lead in the analytical predictions of voltage at later times, Fig. 7(b). Fig. 8 shows that this becomes manifest as a mild warping and planar rotation of the trajectories in phase space when comparing the

measurements to predictions. In Fig. 7(c), it is seen that the spectral distribution of the displacement in time is accurately reconstructed by the analytical approach. The lowest-order harmonic gradually approaches a vanishing point since the snap-through oscillations undergo a significant slowing down prior to the bifurcation in the global dynamic behaviors that results in intrawell oscillations [46]. Unfortunately, the peak reduction in the spectral components in time, such as that around time $t = 0.83$ s, cannot be effectively post-processed using the SFFT because the windowed computation requires a finite number of samples across which to compute reliable data.

Fig. 9 presents a comprehensive assessment of the net converted energies realized by the snap-through dynamics as predicted by the analytical approach (curves) and measured in the experiments (points) for each case of magnet spacing distance Δ considered. The insets show the limiting initial velocities at which snap-through is triggered, which is essential information to reproduce by the analysis to enable its successful utilization for bistable harvester development. Indeed, as seen in each inset of Fig. 9 the predictions accurately identify the initial velocities that are necessary to induce the snap-through vibration in the experimental systems. Moreover, considering each sub-figure in full, the analytical results faithfully estimate the measured net converted energies and also correctly reproduce the particular dependence of energy on the variation of impulse strength (initial velocity). The impulses accounted for by the data of Fig. 9 represent the activation of snap-through dynamics lasting only one up to nearly 20 cycles of transient vibration. Considering the range of initial velocities shown in Fig. 9, the corresponding range of initial impulse energies, $\sim \dot{x}_0^2$, varies by two orders of magnitude. Within this range, the analytical tool provides a high degree of accuracy towards predicting the converted energy, lending strong support and validation to the analytical development and its utilization for bistable energy harvesters in practice.

8. Conclusions

The prevalence of impulsive energies in environments where the energy capture and conversion may facilitate self-powered electronic systems is strong motivation to investigate effective vibration energy harvesting devices which are

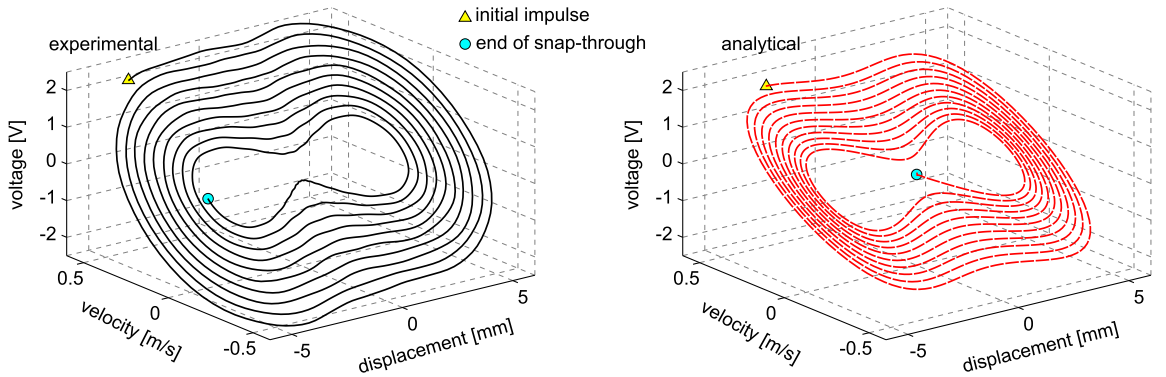

Fig. 8. Phase space comparison of the impulse-excited response shown in Fig. 7. At left are measurements, at right the analytical predictions. The triangles denote the point in the phase space of the initial impulse while the circles denote the end of the snap-through regime.

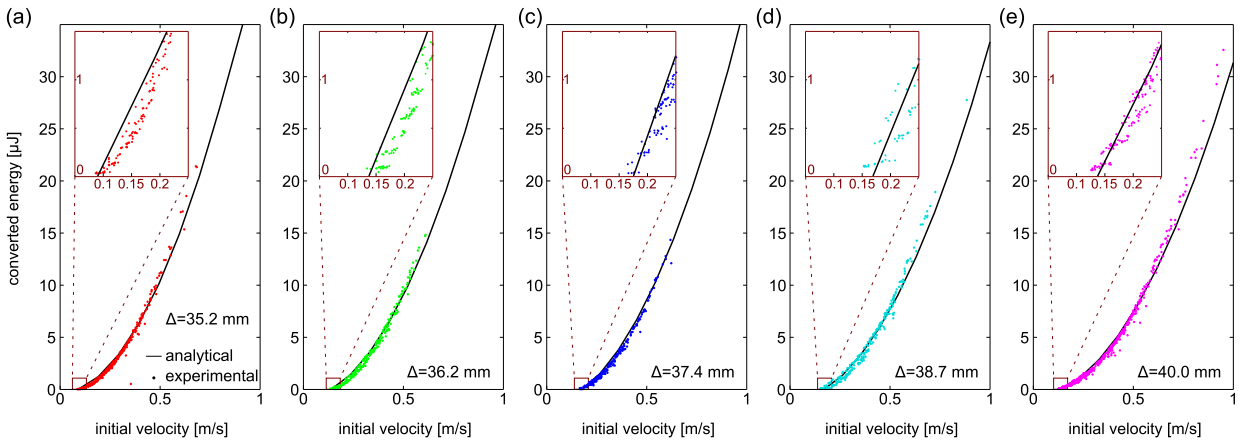

Fig. 9. Comparison of the net converted energies for the snap-through vibration regime as predicted analytically (curves) and measured experimentally (points). The magnet spacing distance Δ varies from (a) 35.2 mm, (b) 36.2 mm, (c) 37.4 mm, (d) 38.7 mm, and finally to (e) 40.0 mm.

particularly sensitive to such excitation. While previous studies have shown that bistable energy harvesters may be beneficial in these environments, an efficient and accurate analytical tool to guide their development and deployment has yet to be created, largely due to the strongly nonlinear and transient nature of the system dynamics. This study addresses this critical need by the development of an analytical approach that faithfully predicts the transient electrodynamic behaviors of impulsively excited bistable energy harvesters. The analytical method is found to provide an accurate indication of the net energy conversion in the snap-through dynamic regime when compared to results obtained through direct simulation of the governing equations. Small overpredictions occur at high initial velocities (high impulse energies) while the approach underpredicts the energy conversion potential of bistable harvesters for very low initial velocities which are only slightly sufficient to trigger the favorable snap-through dynamics. An extensive experimental validation is conducted to examine the accuracy of the analytical predictions across a large range of practical bistable harvester designs and exciting impulse strengths. The fidelity of the analytical results is verified from the excellent agreement with the measured data, both in terms of the transient dynamical trajectories as well as the net energy conversion for a given exciting impulse. From the rigorous numerical and experimental validations, the analytical approach provides a solid foundation upon which to develop optimal bistable energy harvesters for impulsive excitation environments. Moreover, the new analytical development more broadly elucidates the relative susceptibilities of bistable structures to impulse-like excitations, such as those that may result from blasts, impacts, or shocks.

Acknowledgments

This work is supported in part by the National Natural Science Foundation of China (No. 51475356), the Chinese Scholarship Council (CSC), and the University of Michigan Collegiate Professorship.

References

[1] S. Roundy, On the effectiveness of vibration-based energy harvesting, *Journal of Intelligent Material Systems and Structures* 16 (2005) 809–823.
[2] S. Pobering, N. Schwesinger, Power supply for wireless sensor systems, *Proceedings of the IEEE SENSORS 2008 Conference*, Lecce, Italy, 2008, pp. 685–688.
[3] E.M. Yeatman, Energy harvesting from motion using rotating and gyroscopic proof masses, *Proceedings of the Institution of Mechanical Engineers, Part C: Journal of Mechanical Engineering Science* 222 (2008) 27–36.
[4] M.F. Daqaq, Transduction of a bistable inductive generator driven by white and exponentially correlated Gaussian noise, *Journal of Sound and Vibration* 330 (2011) 2554–2564.
[5] Q. He, M.F. Daqaq, Electric load optimization of a nonlinear mono-stable duffing harvester excited by white noise, *Meccanica* http://dx.doi.org/10.1007/s11012-015-0289-7.
[6] M.F. Daqaq, Response of uni-modal duffing-type harvesters to random forced excitations, *Journal of Sound and Vibration* 329 (18) (2010) 3621–3631.
[7] S.C. Stanton, B.P. Mann, B.A.M. Owens, Melnikov theoretic methods for characterizing the dynamics of the bistable piezoelectric inertial generator in complex spectral environments, *Physica D: Nonlinear Phenomena* 241 (2012) 711–720.
[8] J. Scruggs, P. Jacob, Harvesting ocean wave energy, *Science* 323 (2009) 1176–1178.
[9] J.T. Scruggs, Multi-objective optimal causal control of an ocean wave energy converter in random waves, *Proceedings of IEEE OCEANS 2011*, Waikoloa, H, 2011.
[10] Z. Zhang, H. Xiang, Z. Shi, Modeling on piezoelectric energy harvesting from pavements under traffic loads, *Journal of Intelligent Material Systems and Structures* http://dx.doi.org/10.1177/1045389 × 15575081.
[11] A. Erturk, Piezoelectric energy harvesting for civil infrastructure system applications: moving loads and surface strain fluctuations, *Journal of Intelligent Material Systems and Structures* 22 (2011) 1959–1973.
[12] K. Ylli, D. Hoffmann, A. Willmann, P. Becker, B. Folkmer, Y. Manoli, Energy harvesting from human motion: exploiting swing and shock excitations, *Smart Materials and Structures* 24 (2015) 025029.
[13] K. Suhaimi, R. Ramlan, A. Putra, A combined softening and hardening mechanism for low frequency human motion energy harvesting application, *Advances in Acoustics and Vibration* (2014) 217032.
[14] M.A. Karami, D.J. Inman, Controlled buckling of piezoelectric beams for direct energy harvesting from passing vehicles, *Proceedings of the ASME 2012 International Design Engineering Technical Conferences and Computers and Information in Engineering Conference*, Chicago, IL, USA, 2012, pp. DETC2012-71022.
[15] A. Stacoff, C. Diezi, G. Luder, E. Stüssi, I.A. Kramers-de Quervain, Ground reaction forces on stairs: effects of stair inclination and age, *Gait and Posture* 21 (2005) 24–38.
[16] A.M. Wickenheiser, E. Garcia, Broadband vibration-based energy harvesting improvement through frequency up-conversion by magnetic excitation, *Smart Materials and Structures* 19 (2010) 065020.
[17] L. Tang, Y. Yang, C.-K. Soh, Improving functionality of vibration energy harvesters using magnets, *Journal of Intelligent Material Systems and Structures* 23 (2012) 1433–1449.
[18] M.A. Karami, J.R. Farmer, D.J. Inman, Parametrically excited nonlinear piezoelectric compact wind turbine, *Renewable Energy* 50 (2013) 977–987.
[19] M.F. Daqaq, R. Masana, A. Erturk, D.D. Quinn, On the role of nonlinearities in vibratory energy harvesting: a critical review and discussion, *Applied Mechanics Reviews* 66 (2014) 040801.
[20] F. Lakrad, M. Belhaq, Periodic solutions of strongly non-linear oscillators by the multiple scales method, *Journal of Sound and Vibration* 258 (2002) 677–700.
[21] S.B. Yuste, J.D. Bejarano, Improvement of a Krylov–Bogoliubov method that uses Jacobi elliptic functions, *Journal of Sound and Vibration* 139 (1990) 151–163.
[22] S.B. Yuste, "Cubication" of non-linear oscillators using the principle of harmonic balance, *International Journal of Non-Linear Mechanics* 27 (1992) 347–356.
[23] L. Cveticanin, An approximate solution for a system of two coupled differential equations, *Journal of Sound and Vibration* 152 (1992) 375–380.
[24] M.A. Al-Shudeifat, Amplitudes decay in different kinds of nonlinear oscillators, *Journal of Vibration and Acoustics* 137 (2015) 031012.
[25] C. Zhang, R.L. Harne, B. Li, K.W. Wang, Reconstructing the transient, dissipative dynamics of a bistable Duffing oscillator with an enhanced averaging method and Jacobian elliptic functions, *International Journal of Non-Linear Mechanics* 79 (2016) 26–37.

[26] V.T. Coppola, R.H. Rand, Averaging using elliptic functions: approximation of limit cycles, *Acta Mechanica* 81 (1990) 125–142.
[27] V.T. Coppola, R.H. Rand, *Macsyma program to implement averaging using elliptic functions*, *Computer Aided Proofs in Analysis*, Springer, New York, 1991, 71–89.
[28] M. Belhaq, F. Lakrad, Prediction of homoclinic bifurcation: the elliptic averaging method, *Chaos, Solitons and Fractals* 11 (2000) 2251–2258.
[29] I. Kovacic, M.J. Brennan (Eds.), *The Duffing Equation: Nonlinear Oscillators and their Behaviour*, John Wiley & Sons, Chichester, 2011.
[30] A. Erturk, D.J. Inman, Broadband piezoelectric power generation on high-energy orbits of the bistable Duffing oscillator with electromechanical coupling, *Journal of Sound and Vibration* 330 (2011) 2339–2353.
[31] S.C. Stanton, B.A.M. Owens, B.P. Mann, Harmonic balance analysis of the bistable piezoelectric inertial generator, *Journal of Sound and Vibration* 331 (2012) 3617–3627.
[32] R.L. Harne, K.W. Wang, A review of the recent research on vibration energy harvesting via bistable systems, *Smart Materials and Structures* 22 (2013) 023001.
[33] M. Panyam, R. Masana, M.F. Daqaq, On approximating the effective bandwidth of bi-stable energy harvesters, *International Journal of Non-Linear Mechanics* 67 (2014) 153–163.
[34] N. Kong, D.S. Ha, A. Erturk, D.J. Inman, Resistive impedance matching circuit for piezoelectric energy harvesting, *Journal of Intelligent Material Systems and Structures* 21 (2010) 1293–1302.
[35] R.L. Harne, K.W. Wang, On the fundamental and superharmonic effects in bistable energy harvesting, *Journal of Intelligent Material Systems and Structures* 25 (2014) 937–950.
[36] T. Okabe, T. Kondou, J. Ohnishi, Elliptic averaging methods using the sum of Jacobian elliptic delta and zeta functions as the generating solution, *International Journal of Non-Linear Mechanics* 46 (2011) 159–169.
[37] P.F. Byrd, M.D. Friedmand, *Handbook of Elliptic Integrals for Engineers and Physicists*, Springer-Verlag, Berlin, 1954.
[38] Y. Liao, H.A. Sodano, Structural effects and energy conversion efficiency of power harvesting, *Journal of Intelligent Material Systems and Structures* 20 (2009) 505–514.
[39] Y.C. Shu, I.C. Lien, Efficiency of energy conversion for a piezoelectric power harvesting system, *Journal of Micromechanics and Microengineering* 16 (2006) 2429–2438.
[40] R.L. Harne, K.W. Wang, Prospects for nonlinear energy harvesting systems designed near the elastic stability limit when driven by colored noise, *ASME Journal of Vibration and Acoustics* 136 (2014) 021009.
[41] B.P. Mann, N.D. Sims, On the performance and resonant frequency of electromagnetic induction energy harvesters, *Journal of Sound and Vibration* 329 (2010) 1348–1361.
[42] W. Szemplińska-Stupnicka, J. Rudowski, Steady state in the twin-well potential oscillator: computer simulations and approximate analytical studies, *Chaos* 3 (1993) 375–385.
[43] F.C. Moon, P.J. Holmes, A magnetoelastic strange attractor, *Journal of Sound and Vibration* 65 (1979) 275–296.
[44] S.S. Rao, *Mechanical Vibrations*, 4th ed, Pearson Prentice Hall, Upper Saddle River, New Jersey, 2004.
[45] L.N. Virgin, *Introduction to Experimental Nonlinear Dynamics*, Cambridge University Press, Cambridge, 2000.
[46] L.N. Virgin, R. Wiebe, On damping in the vicinity of critical points, *Philosophical Transactions of the Royal Society A* 371 (2013) 20120426.